MATERIALS SCIENCE

Temperature-resilient solid-state organic artificial synapses for neuromorphic computing

A. Melianas[1]*, T. J. Quill[1†], G. LeCroy[1†], Y. Tuchman[1†], H. v. Loo[1,2†], S. T. Keene[1], A. Giovannitti[1], H. R. Lee[1], I. P. Maria[3], I. McCulloch[3,4], A. Salleo[1]*

Devices with tunable resistance are highly sought after for neuromorphic computing. Conventional resistive memories, however, suffer from nonlinear and asymmetric resistance tuning and excessive write noise, degrading artificial neural network (ANN) accelerator performance. Emerging electrochemical random-access memories (ECRAMs) display write linearity, which enables substantially faster ANN training by array programing in parallel. However, state-of-the-art ECRAMs have not yet demonstrated stable and efficient operation at temperatures required for packaged electronic devices (~90°C). Here, we show that (semi)conducting polymers combined with ion gel electrolyte films enable solid-state ECRAMs with stable and nearly temperature-independent operation up to 90°C. These ECRAMs show linear resistance tuning over a >2× dynamic range, 20-nanosecond switching, submicrosecond write-read cycling, low noise, and low-voltage (±1 volt) and low-energy (~80 femtojoules per write) operation combined with excellent endurance (>10^9 write-read operations at 90°C). Demonstration of these high-performance ECRAMs is a fundamental step toward their implementation in hardware ANNs.

INTRODUCTION

Novel materials and neuromorphic devices are required to address the inability of complementary metal-oxide-semiconductor (CMOS) transistor scaling to meet the increasingly demanding computational density and energy requirements of artificial neural networks (ANNs), particularly in embedded platforms with limited area and power budget (*1*). While substantial progress has been made using crossbar arrays of emerging nonvolatile memories, such as phase-change memory (PCM) (*2*) and resistive random-access memory (ReRAM) (*3*), these technologies present fundamental limitations. The inherently stochastic switching in PCMs (melting and recrystallization) and ReRAMs (filament formation) inevitably causes nonlinear and asymmetric resistance tuning, leading to large write errors that are detrimental for accelerating training in hardware ANNs (*4*, *5*). Electrochemical random-access memories (ECRAMs) (*6*–*9*) on the other hand, where resistive switching is instead controlled by ion insertion from the electrolyte into a semiconductor channel, enable linear resistance switching with low write noise (*9*). While linear resistance switching is not essential for high ANN performance, since symmetry in resistance tuning for potentiation/depression is more critical (*4*), device linearity remains the most straightforward way to fulfill the symmetry requirement. Because of the nearly ideal switching characteristics of ECRAM devices, they have therefore emerged as a promising alternative for analog ANN accelerators.

ECRAMs have been demonstrated using several materials classes: Two-dimensional (2D) materials such as graphene or α-phase molybdenum oxide (α-MoO_3), as well as metal oxides such as lithium titanium oxide (Li_xTiO_2), tungsten oxide (WO_3), or lithium cobalt oxide ($Li_{1-x}CoO_2$), have all been used as channel materials. These demonstrations relied on conventional Li-based battery electrolytes, e.g., lithium phosphorous oxynitride (LiPON) (*7*, *8*) or lithium perchlorate ($LiClO_4$) mixed with polyethylene oxide (PEO) (*10*–*12*). While Li-based ECRAMs have shown promising characteristics, most devices are limited to millisecond write speeds. As an exception, a WO_3 channel combined with LiPON electrolyte was shown to respond to 5-ns write pulses but required 1.5-s write-read delays (*8*), thereby severely limiting the overall speed of the device. While the ultimate speed of Li-based devices is being investigated, the relatively sluggish kinetics of Li intercalation poses a fundamental challenge. In addition, Li reactivity is a concern for compatibility with semiconductor fabrication processes.

In contrast, previously reported organic ECRAMs (*6*, *9*), which relied on proton exchange membranes, such as Nafion (*13*), demonstrated 200-ns switching and <1-μs write-read cycles with endurance to >10^8 write-read events (*9*). Nevertheless, despite promising initial demonstrations (*6*, *9*), organic ECRAMs face several challenges.

Proton exchange membranes require extensive hydration to conduct protons (*13*, *14*). Organic ECRAMs (Fig. 1A) made using poly(3,4-ethylenedioxythiophene) polystyrene sulfonate (PEDOT:PSS) (Fig. 1B) as the channel/gate material and a commercially available perfluorosulfonic acid ionomer membrane (Aquivion; see Materials and Methods) as electrolyte do not exhibit any conductance modulation when operated in moderate (2×10^{-4} mbar) vacuum (Fig. 1C). This limitation renders the use of conventional proton exchange membranes incompatible with dry environments and thus integration into ANN accelerators, which is the first technological challenge. The second technological challenge stems from water evaporation from the proton exchange membrane at the temperatures generated in conventional electronic packaging during device operation (up to ~90°C), which, similarly to vacuum, would impair organic ECRAM functionality. While one could argue that this is not a major impediment as biological neurons are temperature sensitive, microelectronics requires temperature-resilient devices.

In addition, previously reported organic ECRAMs suffer from a limited dynamic range (<2×) between the highest/lowest conductance states when using short (~1 μs or less) write pulses (*9*). While operating

[1]Department of Materials Science and Engineering, Stanford University, Stanford, CA 94305, USA. [2]Zernike Institute for Advanced Materials, University of Groningen, 9747AG Groningen, Netherlands. [3]Department of Chemistry and Centre for Plastic Electronics, Imperial College London, London, UK. [4]King Abdullah University of Science and Technology (KAUST), KAUST Solar Center, Thuwal, Saudi Arabia.
*Corresponding author. Email: armantas.melianas@stanford.edu (A.M.); asalleo@stanford.edu (A.S.)
†These authors contributed equally to this work

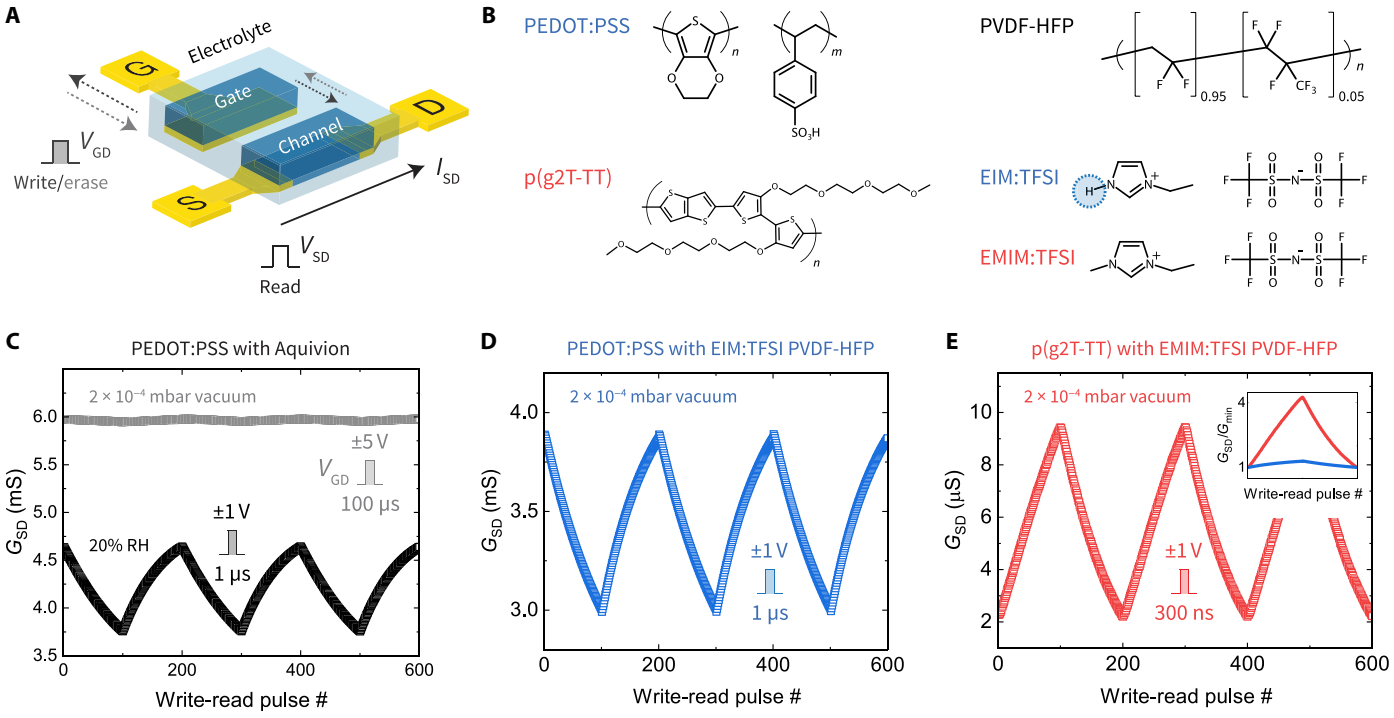

Fig. 1. Organic ECRAMs using ion gels enable submicrosecond switching in vacuum. (**A**) ECRAM device schematic. (**B**) Chemical structures of the channel/gate (left) and electrolyte (right) materials. The blue circle on 1-ethylimidazolium *bis*(trifluoromethylsulfonyl)imide (EIM:TFSI) highlights the hydrogen that renders EIM:TFSI protic. (**C**) Resistive switching characteristics of ECRAM with PEDOT:PSS as the channel/gate material and Aquivion as the electrolyte rapidly deteriorate when going from 20% relative humidity (RH) in N_2 atmosphere (black) to 2×10^{-4} mbar vacuum (gray). (**D**) Cycling of ECRAM with PEDOT:PSS as the channel/gate material and EIM:TFSI poly(vinylidene fluoride-*co*-hexafluoropropylene) (PVDF-HFP) as the electrolyte operating in vacuum. (**E**) Cycling of ECRAM with poly(2-(3,3-*bis*(2-(2-(2-methoxyethoxy)ethoxy)ethoxy)-[2,2-bithiophen]-5-yl)thieno[3,2-*b*]thiophene) [p(g2T-TT)] as the channel/gate material and 1-ethyl-3-methylimidazolium *bis*(trifluoromethylsulfonyl)imide (EMIM:TFSI) PVDF-HFP as the electrolyte operating in vacuum. Inset shows normalized channel conductance $\Delta G_{SD}/G_{min}$ for PEDOT:PSS-based (blue) and p(g2T-TT)-based (red) ECRAMs.

the devices over a small dynamic range is desirable for neuromorphic computing, since it prevents large currents from saturating neurons (e.g., stuck ON cells in PCM arrays), the device dynamic range should be inherently large for improved tolerance to device-to-device variations. For example, if the median ECRAM channel conductance varies across devices in an array, then the lack of conductance range overlap between ECRAMs with a limited dynamic range would be detrimental for ANN computation. In contrast, ECRAMs with a larger dynamic range can be operated over a conductance range common to all devices. A larger dynamic range also improves ECRAM tolerance to write noise, since each state can span a larger conductance range relative to the write noise level. For high ANN accuracy, the targeted dynamic range is >330 times larger than the device write noise (*4*). The improved dynamic range, however, must be attained under submicrosecond write speeds to be relevant for ANN computation. If organic ECRAMs are to be integrated with Si, then these limitations must be overcome while retaining all of the other favorable device metrics, such as write linearity, low write noise, high speed, low switching energy, and high endurance.

RESULTS

Ion gels enable environmentally stable ECRAMs

Here, we demonstrate that solid electrolytes made by infiltrating an electrically insulating polymer with common ionic liquids (Fig. 1B) (*15*) enable organic ECRAMs that are programmable in vacuum at a low voltage of ±1 V using submicrosecond pulses, while still displaying linear resistive switching spanning 100× distinct states (Fig. 1, D and E). Size scaling enables faster switching down to 20 ns (our instrument limit). In this work, we obtain accurate readout of the ECRAM channel conductance G_{SD} as well as the amount of injected charge ΔQ per write pulse by operating the devices using two access transistors (write and read select) (see fig. S1 for the measurement schematic and a more detailed explanation). We use ion gel electrolytes similar to those reported previously (*15*) by mixing the polymeric insulator poly(vinylidene fluoride-*co*-hexafluoropropylene) (PVDF-HFP) with common ionic liquids, such as 1-ethyl-3-methylimidazolium *bis*(trifluoromethylsulfonyl)imide (EMIM:TFSI) or 1-ethylimidazolium *bis*(trifluoromethylsulfonyl)imide (EIM:TFSI) (Fig. 1B).

Intrinsic semiconductor improves dynamic range

While ion gel–based ECRAMs using PEDOT:PSS as the channel/gate material perform as well as previously reported Nafion-based PEDOT:PSS devices had (*6*, *9*) in all respects, they still suffer from a limited dynamic range (<2×) between the highest/lowest conductance states (Fig. 1D). We improve the device dynamic range by replacing PEDOT:PSS with the intrinsic semiconducting polymer poly(2-(3,3-*bis*(2-(2-(2-methoxyethoxy)ethoxy)ethoxy)-[2,2-bithiophen]-5-yl)thieno[3,2-*b*]thiophene) [p(g2T-TT)] (Fig. 1B), which was recently developed to operate in enhancement-mode organic electrochemical transistors (OECTs) (*16*). In contrast to PEDOT:PSS, p(g2T-TT) is highly resistive before electrochemical gating and enables a higher dynamic range (~4×) even under considerably shorter ±1-V 300-ns write

pulses than needed for PEDOT:PSS (Fig. 1, D and E). The large improvement in ECRAM dynamic range is evident when comparing the ECRAM channel conductance ΔG_{SD} normalized by its minimum value $\Delta G_{SD}/G_{min}$ (Fig. 1E, inset). The p(g2T-TT) device linearity and signal-to-noise ratio ($\Delta G^2/\sigma^2 > 100$, where ΔG is the conductance update and σ is its standard deviation) fulfill the requirements for high ANN accuracy (*4*). Hence, p(g2T-TT) outperforms PEDOT:PSS due to its larger dynamic range, lower write energy, and faster switching.

High endurance at elevated temperature

If organic ECRAMs are to be integrated with conventional electronics, then they must demonstrate stable operation during prolonged cycling. To be relevant, endurance tests must also be conducted at temperatures typically reached in packaged semiconductor devices (up to ~90°C). We cycled our ECRAMs in vacuum at 90°C for $>10^9$ write-read events, followed by additional $>10^9$ write-read events at 30°C (Fig. 2, A and B). Our ECRAM cycling characteristics are nearly temperature independent up to 90°C, especially those made with p(g2T-TT) (Fig. 2B). Only some changes are observed following $>2 \times 10^9$ write-read events ($>2 \times 10^7$ full range cycles): Though we observe a 2.4% decrease in the median p(g2T-TT) channel conductance following ~1×10^9 write-read events and a 12.8% decrease after ~2×10^9 write-read events, the cycling behavior remains largely unaffected. While, in the future, it would be desirable to further reduce the observed 12.8% drift in conductance after ~2×10^9 write-read events, the reported device endurance, which is already exceptional within the realm of organic electronics (*17*), is promising for neuromorphic computing implementations: It is indeed competitive with state-of-the-art inorganic resistive switching devices (*18*) and even exceeds that of commercial flash memories (endurance, ~10^6 cycles) (*19*). Our ECRAMs enable a unique combination of high endurance ($>2 \times 10^9$ write-read events) and low noise ($\Delta G^2/\sigma^2 > 100$).

Temperature-stable switching

At elevated temperature, following ~1×10^9 write-read events, the p(g2T-TT) ECRAMs display nearly temperature-independent operation

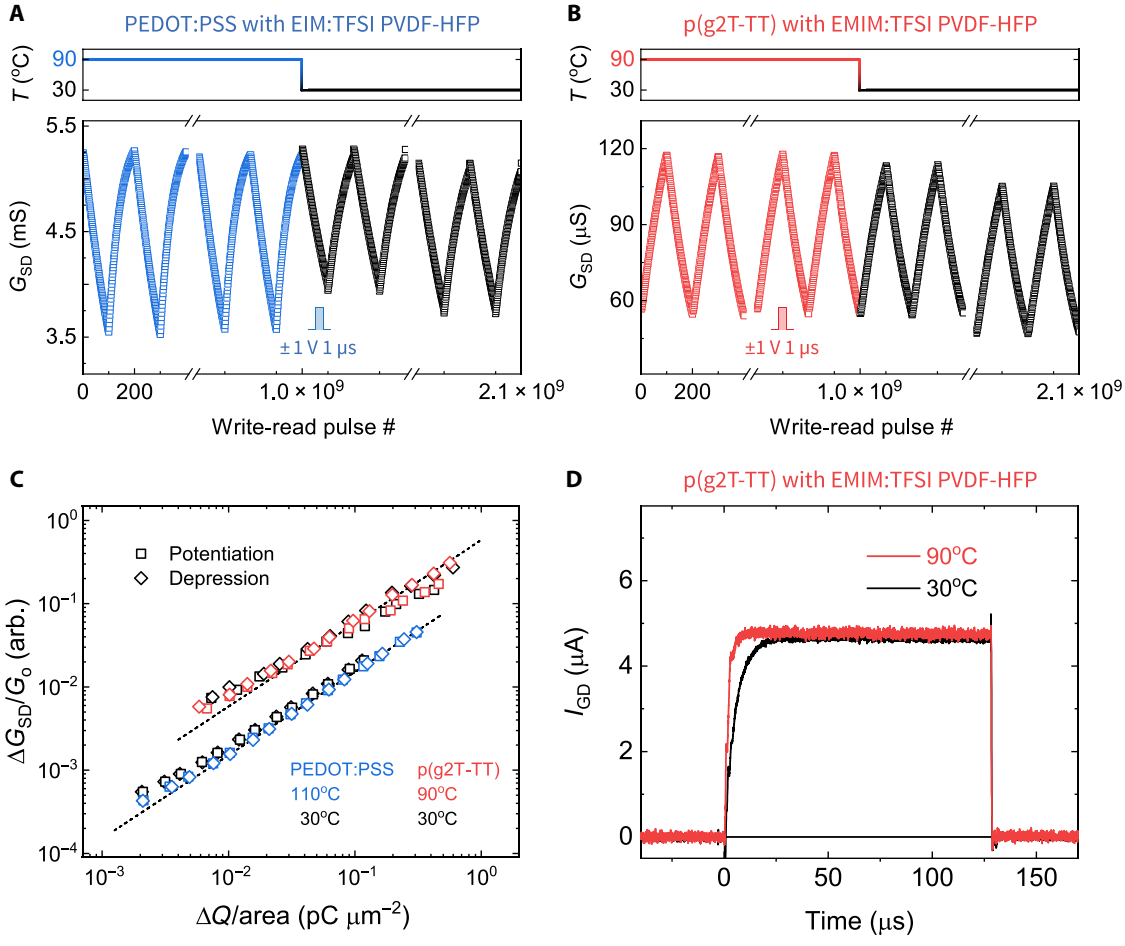

Fig. 2. Temperature-stable switching of organic ECRAMs, $>10^9$ write endurance at 90°C, and temperature-independent write linearity. Endurance of (**A**) PEDOT:PSS EIM:TFSI PVDF-HFP and (**B**) p(g2T-TT) EMIM:TFSI PVDF-HFP devices to $>10^9$ write-read events at 90°C (colored), followed by additional $>10^9$ write-read events at 30°C (black) using ±1-V 1-µs pulses. (**C**) Normalized synaptic weight update $\Delta G_{SD}/G_o$ dependence on injected charge ΔQ per area per write pulse. The dependence is linear at 30°C and at higher temperatures both during potentiation (squares) and depression (diamonds). The black dashed line is a linear fit. arb. stands for arbitrary units. (**D**) Time-resolved write current I_{GD} measurements reveal a 6% increase in the amount of injected charge per write pulse at elevated 90°C temperature (red) compared to 30°C (black). All measurements were performed under 2×10^{-4} mbar vacuum.

with only a 3% increase in the mean channel conductance and only 4% increase in dynamic range compared to room temperature (Fig. 2B). p(g2T-TT) has superior temperature stability in comparison to PEDOT:PSS (9% increase in dynamic range; Fig. 2A). While these small nonidealities do not appreciably affect the functionality of our ECRAMs, understanding their temperature behavior is important for future device design.

The increase in dynamic range with increasing temperature can be understood by recording the amount of injected charge ΔQ per write pulse and the corresponding conductance update per write pulse ΔG_{SD} (fig. S2). To directly compare PEDOT:PSS and p(g2T-TT), which have different absolute conductance, we normalize ΔG_{SD} by the median channel conductance G_o at 30°C. We find that the scaling of $\Delta G_{SD}/G_o$ versus ΔQ is linear and temperature independent (Fig. 2C), the same holds true for ΔG_{SD} versus ΔQ (see fig. S2). These results suggest that the increase in dynamic range with increasing temperature (Fig. 2, A and B) originates from an increase in the amount of injected charge ΔQ per write pulse. Time-resolved measurements of charging during the write pulse (Fig. 2D) confirm this hypothesis. We observe a 6% increase in injected charge at 90°C (Fig. 2D), which is commensurate with the 4% increase in ECRAM dynamic range (Fig. 2B). Figure S2 shows that ΔQ is larger at elevated temperature regardless of pulse duration, whereas note S1 describes why carrier mobility in the ECRAM channel is nearly temperature independent in the investigated 30° to 90°C range.

The increasing charging rate at higher temperature (Fig. 2D), particularly at shorter time scales, suggests that the increase in injected charge is due to an increase in the conductivity of the electrolyte layer (*20*, *21*), allowing more charge to pass to the channel during the programming pulse. Selecting electrolytes with weaker temperature dependence of their conductivity will mitigate changes in resistance tuning with temperature. For the typical array architecture where two devices are used per ANN weight (to represent negative weights) (*5*), as long as the cycling characteristics of all devices in the array shift with temperature by the same amount, ANN computation will remain unaffected.

Low-energy switching at high speed

Figure 2C shows that p(g2T-TT) requires considerably less charge than PEDOT:PSS to attain a similar sized update $\Delta G_{SD}/\Delta G_o$, enabling the use of considerably shorter write pulses, as corroborated earlier in Fig. 1 (D and E). p(g2T-TT) therefore outperforms PEDOT:PSS not only in terms of larger dynamic range (Fig. 1, D and E) and temperature resilience (Fig. 2, A and B) but also speed (Fig. 2C).

To estimate the device write speed limit and evaluate the potential for dense integration into an ANN accelerator, we measured a

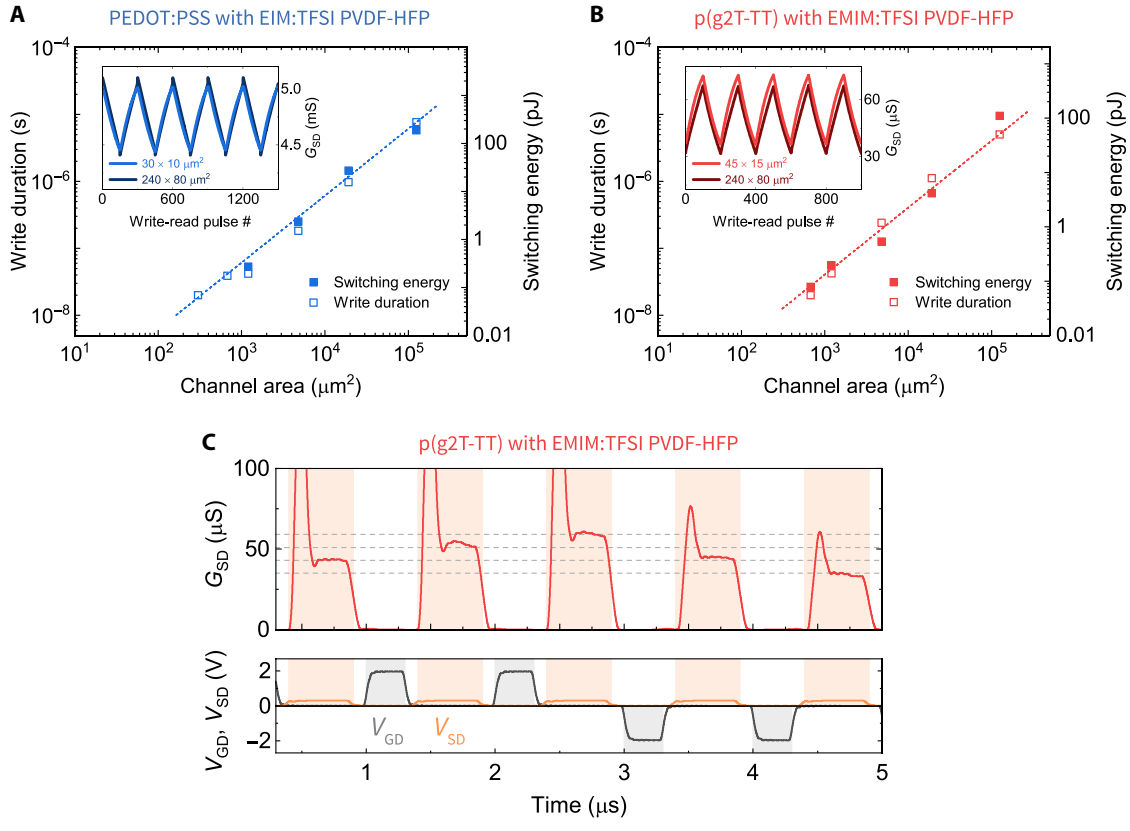

Fig. 3. Device write speed and energy scaling and operation under <1-μs write-read cycles. Switching speed (open squares) and energy (solid squares) scaling of (**A**) PEDOT:PSS EIM:TFSI PVDF-HFP and (**B**) p(g2T-TT) EMIM:TFSI PVDF-HFP devices versus ECRAM channel area. Insets in (A) and (B) show no substantial difference in the switching characteristics of different size devices using scaled write duration. Device modeling (colored dashed lines) predicts that a 1 μm by 1 μm device will enable <20-ns switching with <10 fJ per write switching energy. (**C**) p(g2T-TT) EMIM:TFSI PVDF-HFP device potentiation and depression under ±2-V 200-ns write pulses (gray shaded area), followed by 100-ns write-read delay and +0.3-V 500-ns readout (orange shaded area). The horizontal dashed lines are a guide to the eye. All measurements were performed under 2×10^{-4} mbar vacuum.

series of photolithographically patterned devices down to 30 μm by 30 μm (channel/gate are 30 μm by 10 μm each, separated by 10 μm) and observed no substantial difference in their switching characteristics (Fig. 3, A and B, insets; and see fig. S3 for device-to-device variability). Since the required programming charge decreases with decreasing channel area (*6*, *9*), the same conductance update ΔG_{SD} can be attained in scaled devices using shorter write pulses and correspondingly lower switching energy (Fig. 3, A and B). For example, whereas a 2× conductance modulation can be obtained in a 240 μm by 80 μm p(g2T-TT) channel when using 100× ±1-V 600-ns programming pulses, a similar 2× modulation can be attained in a 45 μm by 15 μm channel (30× smaller area) when using 100× ±1-V 20-ns programming pulses, as shown in Fig. 3B (inset). The corresponding energy cost for the 45 μm by 15 μm channel is ~80 fJ per write, meeting the requirements for low-power neuromorphic computing (*17*, *18*). This low write energy is attained in relatively large devices, emphasizing the inherently low energy consumption of organic ECRAMs.

State retention

The measured state retention of our ECRAMs is of the order of minutes both at 30° and 90°C (fig. S4). This is a major improvement in terms of temperature stability and retention time compared to earlier reports on square millimeter–sized ECRAMs using proton exchange membranes (*6*, *22*), which cannot be heated as their performance would rapidly deteriorate. In contrast to earlier reports, retention of the order of minutes is considerably more difficult to attain in the photolithographically-patterned hundreds of square micron-sized devices used here, because they hold less charge. While the achieved retention is not suitable for inference-only dot-product engines where 10-year retention at 85°C is desired (*18*), our device retention is adequate for applications where ANN learning occurs either continuously (online learning) or where the ANN weights are subsequently transferred to nonvolatile memory (*23*).

Device scaling and submicrosecond operation

Beyond our experimental data, we model the scaling results in Fig. 3 (A and B) using a previously reported model (*24*) that describes ECRAMs as charging capacitors (Fig. 3, A and B, dashed line). We estimate that a 1 μm by 1 μm device will switch faster than 1 GHz using <10 fJ per write.

To ensure low ANN learning accelerator latency, synaptic devices should also exhibit both rapid synaptic weight update and readout during training. Figure 3C shows that our devices can be successfully programmed using <1-μs write-read cycles, which is considerably faster compared to inorganic ECRAMs (*7*, *8*, *10*–*12*). Our ECRAMs thus enable high-temperature operation in dry environments while exhibiting a write speed (20 ns) exceeding that previously reported for Nafion-based ECRAMs (200 ns) (*9*) and having a lower switching energy: For a 45 μm by 15 μm channel, the switching energy is ~2.7 pJ per write for Nafion-based PEDOT:PSS devices, whereas p(g2T-TT) EMIM:TFSI PVDF-HFP devices require only ~80 fJ per write.

It has been recently proposed that fast switching in OECTs occurs when mobile ions are incorporated into the semiconductor channel before electrochemical gating (*25*). X-ray photoelectron spectroscopy (XPS) measurements on our devices confirm that the ionic liquid permeates the semiconductor channel before electrochemical gating (fig. S5). In addition, following deposition of the ion gel electrolyte, the ECRAM channel conductance increases for p(g2T-TT) and decreases for PEDOT:PSS, indicating doping of the semiconducting polymer.

We hypothesize that fast switching, which is unexpected in electrochemical devices, is due to fast-diffusing ions such as protons. We find that PEDOT:PSS devices using the aprotic ionic liquid EMIM:TFSI are barely operational (fig. S6), while those made with the protic (*26*, *27*) EIM:TFSI exhibit excellent performance (Figs. 1 to 3). Similar to aqueous electrolyte–gated organic neuromorphic devices (*6*), we thus hypothesize that protons diffusing in the confined environment of the ion gel and the conjugated polymer microstructure play an important role in the switching of our ion gel–based ECRAMs. Protons are known to diffuse fast and with low activation barriers, especially in hydrogen-bonded networks, where the Grotthuss mechanism is active (*28*). p(g2T-TT) devices, on the other hand, show excellent performance with both EMIM:TFSI-based (Figs. 1 to 3) and EIM:TFSI-based ion gels (fig. S6), suggesting the need for a more detailed understanding of the switching mechanisms and their relationship to proton transport that are beyond the scope of this work.

DISCUSSION

In summary, we fulfill the large number of requirements for efficient neuromorphic computing in a single organic ECRAM device: linear resistance tuning with a >2× dynamic range, fast switching (20 ns), submicrosecond write-read cycling, low-voltage (±1 V) and low-energy (~80 fJ per write) operation, low noise ($\Delta G^2/\sigma^2 > 100$), and excellent endurance both at room temperature and at elevated temperature (>10^9 write-read operations at 90°C). Our materials selection strategy proves to be quite general, as it can be effectively implemented using various ionic liquids and other block copolymers (fig. S7). In contrast, it has been proven difficult to optimize PCMs and ReRAMs across all metrics, such as attaining both low write noise and low current operation, which are needed for scaling to large arrays.

While this work represents a fundamental step toward designing organic ECRAMs to be compatible with fabrication into high-density synaptic arrays, some important challenges remain due to the strict temperature and contamination requirements for integration with CMOS. Alternative fabrication pathways exist for integrating emerging nonvolatile memories with CMOS, such as low-temperature monolithic 3D integration of carbon nanotubes and ReRAMs (*29*), and remain an active area of pursuit to improve such compatibility.

Last, we emphasize that the ECRAM concept is not limited to organic materials. The lessons learned here, such as the importance of mobile species infiltrating the channel before electrochemical gating and possibly relying on proton conduction for fast switching, can also benefit ECRAMs made with other ion intercalation materials such as 2D materials, van der Waals heterostructures, or MXene composites.

MATERIALS AND METHODS

Channel and gate materials

Spin-coating solution of PEDOT:PSS was prepared by adding 6 weight % (wt %) ethylene glycol (Sigma-Aldrich), 0.1 wt % dodecylbenzene sulfonic acid (Sigma-Aldrich) as surfactant, and 1 wt % (3-glycidyloxypropyl) trimethoxysilane (Sigma-Aldrich) as cross-linking agent to an aqueous PEDOT:PSS dispersion (Clevios PH 1000, Heraeus). p(g2T-TT) was synthesized as reported previously (*16*)

and was dissolved in chloroform (3 mg ml^{-1}) at 60°C using a magnetic stir bar for at least 2 hours. Before spin coating, the PEDOT:PSS solution was filtered through a 0.45-μm PVDF membrane (Merck Millipore Ltd.), whereas the p(g2T-TT) solution was filtered through a 0.45-μm glass fiber filter (Kinesis Inc.).

Electrolyte materials

Aquivion D66-25BS electrolyte was obtained from Solvay. Aquivion was chosen because of its weaker conductivity dependence versus relative humidity compared to Nafion. Ionic liquids EMIM:TFSI and EIM:TFSI were purchased from Iolitec (99.5 and 98% grade, respectively). Ionic liquids were baked out in a vacuum oven and subsequently stored in an N_2-filled glovebox. Polymeric insulator PVDF-HFP pellets with an average M_w (weight-average molecular weight) of ~400,000 and an average M_n (number-average molecular weight) of ~130,000 were purchased from Sigma-Aldrich. Ion gels were prepared in ambient by dissolving PVDF-HFP and the ionic liquid (1:4, w/w) in acetone with the following proportions: 17.6 wt % ionic liquid, 4.4 wt % polymer, and 78 wt % solvent. The resulting ion gel solution was stirred at 40°C for at least 30 min and then drop-cast onto the prepatterned organic semiconductor channel/gate.

Device fabrication

ECRAM devices were photolithographically patterned in the same way as reported previously (*9*, *16*). Briefly, metal electrodes (8-nm Ti/50-nm Au) were patterned onto Si wafers coated with 1 μm of SiO_2 using an e-beam evaporator. The wafers were subsequently coated with 1.5 μm of parylene C as the insulating layer, cross-linked with the adhesion promoter 3-(trimethoxysilyl)propyl methacrylate. Following the first parylene C layer, a dilute soap solution (3% Micro-90 in water) was spin-cast on top to prevent the subsequent 1.5 μm of parylene C layer from adhering too strongly. The wafers were then coated with 75 nm of Ti using e-beam evaporation, which was subsequently patterned and dry-etched together with the parylene C layers to define the ECRAM channel, gate, and contact pad regions. The wafer dies were cleaned with isopropanol sonication followed by ultraviolet-ozone cleaning before spin-coating the PEDOT:PSS or p(g2T-TT) layers. The PEDOT:PSS solution was spun on the wafer dies in ambient at 1000 rpm for 2 min and baked at 120°C for 20 min, whereas the p(g2T-TT) solution was spun in an N_2-filled glovebox at 1000 rpm for 1 min and baked at 60°C for 1 min. The top parylene C layer was then peeled off in ambient to confine the organic semiconductor only in the photolithographically defined ECRAM channel and gate regions. The wafer dies were gently rinsed in deionized water to eliminate residual soap and were subsequently dried using a N_2 gun. The ion gel solution was then drop-cast on top, as schematically shown in Fig. 1A.

Device measurements

ECRAMs were measured in a vacuum probe station (LTMP-4, MMR Technologies) at 2×10^{-4} mbar vacuum. Aquivion ECRAM measurements at 20% relative humidity were performed in a glovebox with humidity control (Smart Glovebox, Terra Universal). Device cycling and time-resolved measurements were performed using a pair of waveform generators (33520B and 33522B, 30 MHz, Keysight Technologies) and an oscilloscope (DSOS054A, 500 MHz, Keysight Technologies) controlled using custom LabVIEW software. The circuitry was assembled with commercial off-the-shelf components on a custom-designed printed circuit board and enclosure. The resulting data were analyzed using custom MATLAB scripts. The shortest attainable write pulse duration using our setup is ~20 ns, as used in the section "Low-energy switching at high speed".

SUPPLEMENTARY MATERIALS

Supplementary material for this article is available at http://advances.sciencemag.org/cgi/content/full/6/27/eabb2958/DC1

REFERENCES AND NOTES

1. X. Xu, Y. Ding, S. X. Hu, M. Niemier, J. Cong, Y. Hu, Y. Shi, Scaling for edge inference of deep neural networks. *Nat. Electron.* **1**, 216–222 (2018).
2. G. W. Burr, R. M. Shelby, C. di Nolfo, J. W. Jang, R. S. Shenoy, P. Narayanan, K. Virwani, E. U. Giacometti, B. Kurdi, H. Hwang, in *2014 IEEE International Electron Devices Meeting* (IEEE, 2014), pp. 29.5.1-29.5.4.
3. M. Hu, C. E. Graves, C. Li, Y. Li, N. Ge, E. Montgomery, N. Davila, H. Jiang, R. S. Williams, J. J. Yang, Q. Xia, J. P. Strachan, Memristor-based analog computation and neural network classification with a dot product engine. *Adv. Mater.* **30**, 1705914 (2018).
4. S. Agarwal, S. J. Plimpton, D. R. Hughart, A. H. Hsia, I. Richter, J. A. Cox, C. D. James, M. J. Marinella, in *Proceedings of the International Joint Conference on Neural Networks* (IEEE, 2016), pp. 929–938.
5. H. Tsai, S. Ambrogio, P. Narayanan, R. M. Shelby, G. W. Burr, Recent progress in analog memory-based accelerators for deep learning. *J. Phys. D Appl. Phys.* **51**, 283001 (2018).
6. Y. van de Burgt, E. Lubberman, E. J. Fuller, S. T. Keene, G. C. Faria, S. Agarwal, M. J. Marinella, A. Alec Talin, A. Salleo, A non-volatile organic electrochemical device as a low-voltage artificial synapse for neuromorphic computing. *Nat. Mater.* **16**, 414–418 (2017).
7. E. J. Fuller, F. El Gabaly, F. Léonard, S. Agarwal, S. J. Plimpton, R. B. Jacobs-Gedrim, C. D. James, M. J. Marinella, A. A. Talin, Li-ion synaptic transistor for low power analog computing. *Adv. Mater.* **29**, 1604310 (2017).
8. J. Tang, D. Bishop, S. Kim, M. Copel, T. Gokmen, T. Todorov, S. Shin, K. T. Lee, P. Solomon, K. Chan, W. Haensch, J. Rozen, in *International Electron Devices Meeting, IEDM* (IEEE, 2019), pp. 13.1.1–13.1.4.
9. E. J. Fuller, S. T. Keene, A. Melianas, Z. Wang, S. Agarwal, Y. Li, Y. Tuchman, C. D. James, M. J. Marinella, J. J. Yang, A. Salleo, A. A. Talin, Parallel programming of an ionic floating-gate memory array for scalable neuromorphic computing. *Science* **364**, 570–574 (2019).
10. M. T. Sharbati, Y. Du, J. Torres, N. D. Ardolino, M. Yun, F. Xiong, Low-power, electrochemically tunable graphene synapses for neuromorphic computing. *Adv. Mater.* **30**, 1802353 (2018).
11. C. Sen Yang, D. S. Shang, N. Liu, E. J. Fuller, S. Agrawal, A. A. Talin, Y. Q. Li, B. G. Shen, Y. Sun, All-solid-state synaptic transistor with ultralow conductance for neuromorphic computing. *Adv. Funct. Mater.* **28**, 1804170 (2018).
12. Y. Li, E. J. Fuller, S. Asapu, S. Agarwal, T. Kurita, J. J. Yang, A. A. Talin, Low-voltage, CMOS-free synaptic memory based on Li_XTiO_2 redox transistors. *ACS Appl. Mater. Interfaces* **11**, 38982–38992 (2019).
13. K. A. Mauritz, R. B. Moore, State of understanding of Nafion. *Chem. Rev.* **104**, 4535–4585 (2004).
14. K. D. Kreuer, S. J. Paddison, E. Spohr, M. Schuster, Transport in proton conductors for fuel-cell applications: Simulations, elementary reactions, and phenomenology. *Chem. Rev.* **104**, 4637–4678 (2004).
15. K. H. Lee, M. S. Kang, S. Zhang, Y. Gu, T. P. Lodge, C. D. Frisbie, "Cut and stick" rubbery ion gels as high capacitance gate dielectrics. *Adv. Mater.* **24**, 4457–4462 (2012).
16. A. Giovannitti, D.-T. Sbircea, S. Inal, C. B. Nielsen, E. Bandiello, D. A. Hanifi, M. Sessolo, G. G. Malliaras, I. McCulloch, J. Rivnay, Controlling the mode of operation of organic transistors through side-chain engineering. *Proc. Natl. Acad. Sci. U.S.A.* **113**, 12017–12022 (2016).
17. Y. Van De Burgt, A. Melianas, S. T. Keene, G. Malliaras, A. Salleo, Organic electronics for neuromorphic computing. *Nat. Electron.* **1**, 386–397 (2018).
18. M. Lanza, H.-S. S. P. Wong, E. Pop, D. Ielmini, D. Strukov, B. C. Regan, L. Larcher, M. A. Villena, J. J. Yang, L. Goux, A. Belmonte, Y. Yang, F. M. Puglisi, J. Kang, B. Magyari-Köpe, E. Yalon, A. Kenyon, M. Buckwell, A. Mehonic, A. Shluger, H. Li, T. H. Hou, B. Hudec, D. Akinwande, R. Ge, S. Ambrogio, J. B. Roldan, E. Miranda, J. Suñe, K. L. Pey, X. Wu, N. Raghavan, E. Wu, W. D. Lu, G. Navarro, W. Zhang, H. Wu, R. Li, A. Holleitner, U. Wurstbauer, M. C. Lemme, M. Liu, S. Long, Q. Liu, H. Lv, A. Padovani, P. Pavan, I. Valov, X. Jing, T. Han, K. Zhu, S. Chen, F. Hui, Y. Shi, Recommended methods to study resistive switching devices. *Adv. Electron. Mater.* **5**, 1800143 (2019).
19. C. Zhao, C. Z. Zhao, S. Taylor, P. R. Chalker, Review on non-volatile memory with high-*k* dielectrics: Flash for generation beyond 32 nm. *Materials (Basel).* **7**, 5117–5145 (2014).
20. H. Tokuda, K. Hayamizu, K. Ishii, M. A. B. H. Susan, M. Watanabe, Physicochemical properties and structures of room temperature ionic liquids. 2. variation of alkyl chain length in imidazolium cation. *J. Phys. Chem. B* **109**, 6103–6110 (2005).

21. S. Zhang, K. H. Lee, C. D. Frisbie, T. P. Lodge, Ionic conductivity, capacitance, and viscoelastic properties of block copolymer-based ion gels. *Macromolecules* **44**, 940–949 (2011).
22. S. T. Keene, A. Melianas, Y. van de Burgt, A. Salleo, Mechanisms for enhanced state retention and stability in redox-gated organic neuromorphic devices. *Adv. Electron. Mater.* **5**, 1800686 (2019).
23. S. Ambrogio, P. Narayanan, H. Tsai, R. M. Shelby, I. Boybat, C. Di Nolfo, S. Sidler, M. Giordano, M. Bodini, N. C. P. Farinha, B. Killeen, C. Cheng, Y. Jaoudi, G. W. Burr, Equivalent-accuracy accelerated neural-network training using analogue memory. *Nature* **558**, 60–67 (2018).
24. S. T. Keene, A. Melianas, E. J. Fuller, Y. van de Burgt, A. A. Talin, A. Salleo, Optimized pulsed write schemes improve linearity and write speed for low-power organic neuromorphic devices. *J. Phys. D Appl. Phys.* **51**, 224002 (2018).
25. G. D. Spyropoulos, J. N. Gelinas, D. Khodagholy, Internal ion-gated organic electrochemical transistor: A building block for integrated bioelectronics. *Sci. Adv.* **5**, eaau7378 (2019).
26. N. Yaghini, L. Nordstierna, A. Martinelli, Effect of water on the transport properties of protic and aprotic imidazolium ionic liquids-an analysis of self-diffusivity, conductivity, and proton exchange mechanism. *Phys. Chem. Chem. Phys.* **16**, 9266–9275 (2014).
27. T. L. Greaves, C. J. Drummond, Protic ionic liquids: Properties and applications. *Chem. Rev.* **108**, 206–237 (2008).
28. X. Wu, J. J. Hong, W. Shin, L. Ma, T. Liu, X. Bi, Y. Yuan, Y. Qi, T. W. Surta, W. Huang, J. Neuefeind, T. Wu, P. A. Greaney, J. Lu, X. Ji, Diffusion-free Grotthuss topochemistry for high-rate and long-life proton batteries. *Nat. Energy* **4**, 123–130 (2019).
29. M. M. S. Aly, M. Gao, G. Hills, C. S. Lee, G. Pitner, M. M. Shulaker, T. F. Wu, M. Asheghi, J. Bokor, F. Franchetti, K. E. Goodson, C. Kozyrakis, I. Markov, K. Olukotun, L. Pileggi, E. Pop, J. Rabaey, C. Ré, H. S. P. Wong, S. Mitra, Energy-efficient abundant-data computing: The N3XT 1,000. *Computer* **48**, 24–33 (2015).
30. B. Tang, S. P. White, C. D. Frisbie, T. P. Lodge, Synergistic increase in ionic conductivity and modulus of triblock copolymer ion gels. *Macromolecules* **48**, 4942–4950 (2015).
31. G. Greczynski, T. Kugler, M. Keil, W. Osikowicz, M. Fahlman, W. R. Salaneck, Photoelectron spectroscopy of thin films of PEDOT-PSS conjugated polymer blend: A mini-review and some new results. *J. Electron Spectros. Relat. Phenomena* **121**, 1–17 (2001).
32. A. Gumyusenge, D. T. Tran, X. Luo, G. M. Pitch, Y. Zhao, K. A. Jenkins, T. J. Dunn, A. L. Ayzner, B. M. Savoie, J. Mei, Semiconducting polymer blends that exhibit stable charge transport at high temperatures. *Science* **362**, 1131–1134 (2018).

Acknowledgments: We thank S. Taheri from the System Prototyping Facility at Stanford University for help in improving the electrical device testing setup. We thank C. Oldani and C. McGuiness at Solvay for providing the Aquivion electrolyte. **Funding:** A.M. acknowledges support from the Knut and Alice Wallenberg Foundation (KAW 2016.0494) for Postdoctoral Research at Stanford University. T.J.Q. and G.L. acknowledge support from the NSF Graduate Research Fellowship Program under grant DGE-1656518. A.G. and A.S. acknowledge funding from the TomKat Center for Sustainable Energy at Stanford University. A.S. and S.T.K. acknowledge financial support from the NSF and the Semiconductor Research Corporation, E2CDA award no. 1739795. In addition, S.T.K. acknowledges the Stanford Graduate Fellowship fund for support. Y.T. acknowledges support from the NSF, award DMR#1808401. Part of this work was performed at the nano@stanford laboratories, supported by the NSF under award ECCS-1542152. **Author contributions:** A.M. conceived the idea and led the project under A.S.'s supervision. A.M. wrote and A.S. edited the manuscript. A.M., H.v.L., G.L., and T.J.Q. prototyped and characterized ECRAM devices. T.J.Q., S.T.K., and A.M. measured and analyzed XPS data. Y.T. designed, assembled, and programmed the electrical device testing setup. Y.T. and A.M. fabricated patterned dies for ECRAM measurements. H.R.L. assisted with the preparation of the ion gels. A.G. and I.P.M. provided p(g2T-TT) under I.M.'s supervision. All authors commented on the manuscript. **Competing interests:** The authors declare that they have no competing interests. **Data and materials availability:** All data needed to evaluate the conclusions in the paper are present in the paper and/or the Supplementary Materials. The data and code that support the findings of this study may be requested from the corresponding authors.

Submitted 13 February 2020
Accepted 20 May 2020
Published 3 July 2020
10.1126/sciadv.abb2958

Citation: A. Melianas, T. J. Quill, G. LeCroy, Y. Tuchman, H. v. Loo, S. T. Keene, A. Giovannitti, H. R. Lee, I. P. Maria, I. McCulloch, A. Salleo, Temperature-resilient solid-state organic artificial synapses for neuromorphic computing. *Sci. Adv.* **6**, eabb2958 (2020).